Palaeogeography, Palaeoclimatology, Palaeoecology 533 (2019) 109230

Contents lists available at ScienceDirect

Palaeogeography, Palaeoclimatology, Palaeoecology

journal homepage: www.elsevier.com/locate/palaeo

Large dry-humid fluctuations in Asia during the Late Cretaceous due to orbital forcing: A modeling study

Jian Zhang[a,*], Yonggang Liu[b], Xiaomin Fang[a,c,d], Chengshan Wang[e], Yibo Yang[a,c]

[a] CAS Key Laboratory of Continental Collision and Plateau Uplift, Institute of Tibetan Plateau Research, Chinese Academy of Sciences (CAS), Beijing 100101, China
[b] Department of Atmosphere and Ocean Sciences, School of Physics, Peking University, Beijing 100871, China
[c] CAS Center for Excellence in Tibetan Plateau Earth Sciences, Chinese Academy of Sciences (CAS), Beijing 100101, China
[d] University of Chinese Academy of Sciences, Beijing 100049, China
[e] State Key Laboratory of Biogeology and Environmental Geology, School of Earth Sciences and Resources, China University of Geosciences Beijing, Beijing 100083, China

ARTICLE INFO

Keywords:
Asian aridity
Orbital cycle
Paleoclimate modeling
Greenhouse climate

ABSTRACT

Cretaceous stratigraphy in the mid- to low-latitude Asia indicates that the climate was overall dry with large variations in aridity in timescales of 1–100 ka, different from the present-day monsoonal humid climate. To identify the possible mechanism for such variation, we modeled the Late Cretaceous climate using a fully coupled atmosphere-ocean general circulation model (AOGCM), Community Earth System Model version 1.2 (CESM1.2), under different CO_2 concentrations and orbital configurations. The simulation results show that the mid- to low-latitude Asia was generally dry during that time, consistent with reconstructions. The arid area decreases and the semi-arid area increases with the increase of CO_2 concentration, but the change in total area is small even when CO_2 is increased by 8 folds. In contrast, the area of dryland can increase by ~67% or 500% depending on how dryness is defined, when the orbital configuration changes from one in which the northern hemispheric summer receives the most solar insolation to one in which it receives the least solar insolation. Therefore, the mid- to low-latitude Asia was likely going through dramatic dry-humid cycles at orbital timescale during the Late Cretaceous, similar to the Saharan region during the Late Miocene-Pleistocene.

1. Introduction

Proxies from oceanic sediments reveal that climate during the Cretaceous (144–66 million years ago (Ma)) was overall significantly warmer than that of the present day (Bornemann et al., 2008; Wilson et al., 2002), consistent with the paleobotanical and paleontological evidence on land (Herman and Spicer, 1996; Spicer et al., 2008). The tropical sea surface temperatures (SSTs) could reach 33–36 °C (Wilson et al., 2002; Forster et al., 2007), and the polar surface temperatures were above 0 °C (Huber et al., 2002; Jenkyns et al., 2004). The warm climate has been generally attributed to the much higher concentration of atmospheric carbon dioxide (CO_2) than today, probably 2–14 times the pre-industrial value (Bice and Norris, 2002; Huber et al., 2002). Besides the difference in climate, the distribution of arid regions in Asia was very different from that of today. Eolian and gypsiferous deposits were widely distributed in the mid- to low-latitude Asia (Fang et al., 2016; Hasegawa et al., 2009, 2012; Jiang et al., 2004, 2008), indicating that the region was arid/semi-arid then (Fang et al., 2016; Hasegawa et al., 2012).

The aridity in the mid- to low-latitude Asia is consistent with the paleo-wind reconstructions, which suggests that the region was dominated by the subtropical high-pressure system (Hasegawa et al., 2012; Jiang et al., 2001, 2008). Previous modeling study demonstrated that the evaporation was in excess of precipitation in that region (Chen et al., 2013), consistent with the reconstructions. The position of the subtropical high and monsoonal precipitation, however, can be affected by both greenhouse gas (represented herein simply by CO_2) concentration and the orbital configuration (Jiang et al., 2015). Significant reduction of CO_2 might have occurred during the late Cretaceous as suggested by the rapid temperature drop at a few locations. For example, changes in both $\delta^{18}O$ of paleosoil carbonate (Gao et al., 2015) and abundance of spore/pollen (Wang et al., 2013) at Songliao Basin in northeast China indicate a cooling of ~8 °C near the Campanian/Maastrichtian boundary (~70 Ma); an even more significant temperature drop might have occurred in the Russian Far East during the same period (Zakharov et al., 1999). Also in Songliao Basin, the orbital signal in the deposits has been detected, suggesting its impact on the Cretaceous Asian climate (Wu et al., 2014). Therefore, the extent of arid

* Corresponding author.
E-mail address: zhangjian@itpcas.ac.cn (J. Zhang).

https://doi.org/10.1016/j.palaeo.2019.06.003
Received 15 January 2019; Received in revised form 15 May 2019; Accepted 4 June 2019
Available online 06 June 2019
0031-0182/

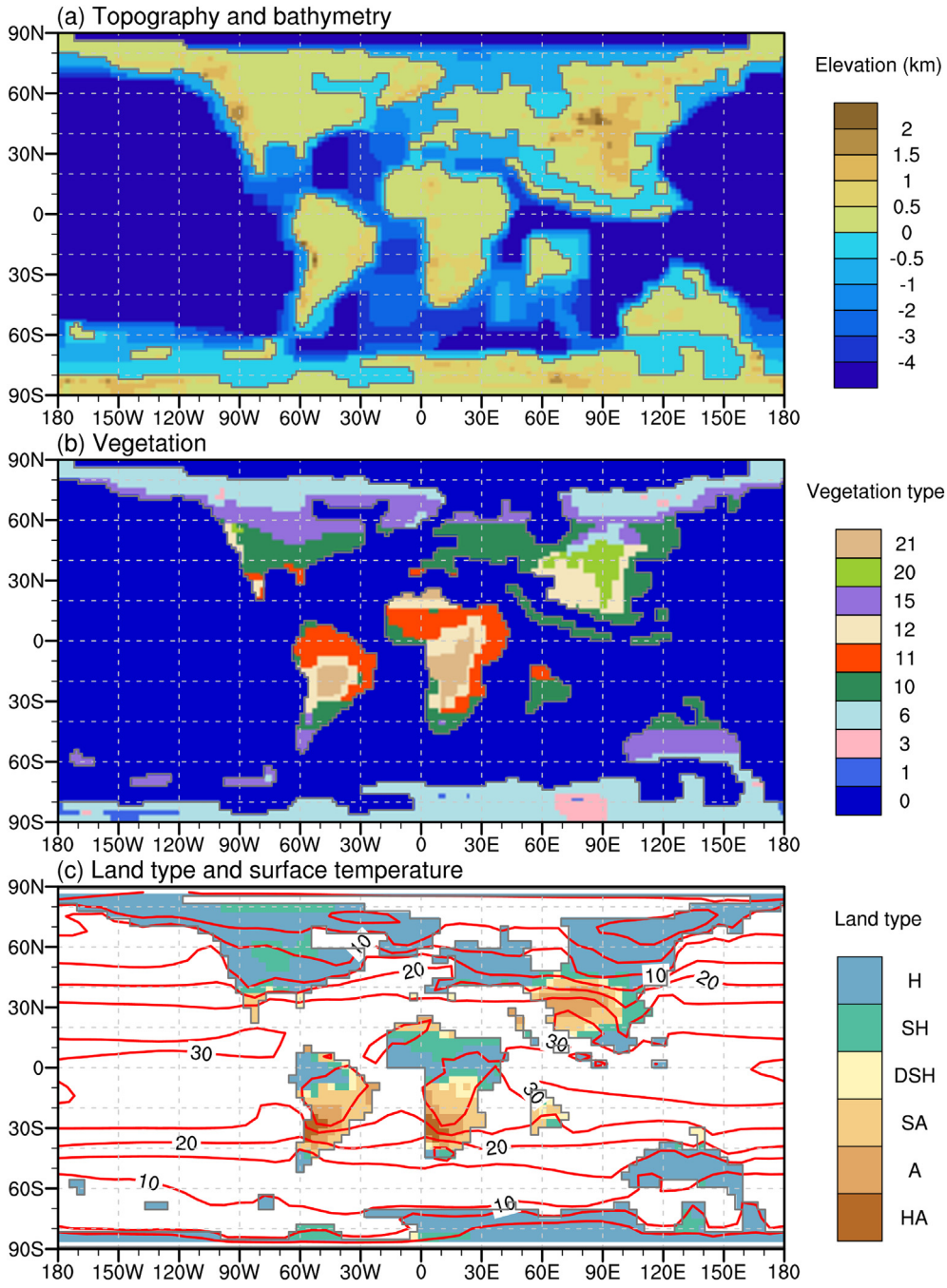

Fig. 1. The global paleogeography (a, units: m), the vegetation (b) of the Late Campanian-Early Maastrichtian (~70 Ma, Sewall et al., 2007), and distribution of climate types (c, shadings) and annual mean surface temperature (c, contours, units: °C) with the interval of 5 °C for the experiments x2. In the vegetation, the numbers 0 is for the ocean, 1 for the land ice, 3 for the high altitude/latitude evergreen conifer closed canopy forest, 6 for the high altitude/latitude mixed forest with equal percentage broad vs needle leaf and evergreen vs deciduous, 10 for the closed canopy, broad leaved, moist evergreen forest, 11 for the closed canopy, broad leaved, dry deciduous forest, 12 for the savanna (dry, low understory with sparse broad leaved overstory), 15 for the high altitude/latitude moist, open canopy evergreen forest with shrub understory, 20 for the wet or cool shrubland (evergreen), and 21 for the dry or warm shrubland (deciduous), which is the same as the Land Surface Model (LSM) vegetation types. For the land types (c), H is for the humid type, SH for the semi-humid type, DSH for dry subhumid type, SA for the semi-arid type, A for the arid type, and HA for the hyper-arid type, respectively.

region might have shifted or oscillated during this period due to the change of both CO_2 and orbital parameters.

Indeed, the paleoenvironmental and paleoclimatic evidence in the Gobi Basin (see Fig. 2 for its location) indicates that the region changed from semi-humid to semi-arid during the Campanian (83.6–72.1 Ma) and then returned to relative humid in the early Masstrichtian (~70 Ma; Hasegawa et al., 2009; Jerzykiewicz and Russell, 1991). The draa-wet-interdraa cycles with period of 10^3–10^5 years were also recognized in the Ordos Basin (Jiang et al., 2004), and have been assumed to be closely related to the Earth's orbital cycles. The oscillatory nature of records at $< 10^6$-year timescales precludes the influence of topographic evolution as a major driving force. Previous modeling study showed that reduction of CO_2 could enlarge the arid region in Asia (Chen et al., 2013). This seems to be consistent with records in the Gobi Basin where the overall trend of dryness corresponded reasonably well with the decreasing of CO_2 concentration between ~90–72 Ma, and the possible sharp return to high value near 70 Ma (Wang et al., 2014). However, to the best of our knowledge, the influence of orbital configurations on the aridity of Asia during the late Cretaceous has not been studied using climate model simulations.

Here we model the Late Cretaceous climate under different CO_2 levels and orbital configurations with an atmosphere-ocean general circulation model (AOGCM), with a specific focus on the aridity of Asia. Unlike the previous study by Chen et al. (2013) who estimated the aridity by simply comparing the precipitation and evaporation, we characterize the aridity of land more quantitatively by computing the aridity index (Feng and Fu, 2013). As will be described in what follows, the change of orbital configuration has a much larger impact on the aridity of Asia than even an 8-fold change of CO_2 concentration. The remainder of this paper is organized as follows: Section 2 presents the model and methods we used and the experimental design. The model results are given in Section 3. The mechanism is analyzed in Section 4.

And finally, the conclusion is provided in Sections 5.

2. Model and methods

2.1. The climate model

In this study, the Community Earth System Model version1.2 (CESM1.2) developed by National Center of Atmospheric Research (NCAR) is employed. CESM1.2 has seven components: atmosphere, ocean, land, river runoff, sea ice, land ice, and ocean wave, which interact with each other through a coupler (Vertenstein et al., 2013). Only the first 5 components are needed in the current study since the land ice was absent for the period of interest and we are not interested in the ocean waves.

The atmospheric module, Community Atmosphere Model version 4 (CAM4, Neale et al., 2013), is run at a horizontal resolution of T31 (~3.75° × 3.75°) with 26 levels in the vertical. The land module, Community Land Model version 4.0 (CLM4.0, Lawrence et al., 2012), has the same horizontal resolution as the CAM4, but only has 10 levels in the vertical. A river transport model with the default resolution (0.5° × 0.5°) routes all runoff to the oceans. River runoff direction at each land grid point is computed based on surface topography such that flow runs downhill and prevents interior drainage loops. The ocean module, Parallel Ocean Model (POP2, Danabasoglu et al., 2012), employs a gx3v7 grid which has 116 and 100 grid points in the meridional and zonal directions, respectively, and 60 levels in the vertical. The sea ice module, Community Sea Ice Model (Hunke and Lipscomb, 2008) is run on the same horizontal grid as POP2. This low resolution version of CESM/CCSM can yield a realistic simulation of the present climate (Shields et al., 2012), and has also been used to simulate deep paleoclimate (e.g. Fiorella and Sheldon, 2017; Frieling et al., 2017).

2.2. Experimental design

The paleogeography and paleovegetation are taken from Sewall et al. (2007), who provided four Cretaceous time slices, with a resolution of 2.8° × 2.8°; the ~70 Ma geography and vegetation are used in this study (Fig. 1a and b). To make sure that the ocean module is able to converge, the paleogeography was adjusted slightly following the manual provided by NCAR (Rosenbloom et al., 2011): the topography and bathymetry are smoothed to remove abrupt changes; some very small land patches are removed; the small bay (~170–180°E) rimming the paleo-Arctic Ocean is replaced with land grids. In addition, the mid-ocean ridges in the ocean interior, especially those in the Pacific Ocean are removed. They have little influence on the surface climate (e.g. Liu et al., 2013) but may cause convergence problem.

The CO_2 concentration during the Cretaceous is difficult to constrain and suffers from large uncertainties. It could have varied between 2 and 14 times the pre-industrial level with low resolution in time (Bice and Norris, 2002; Huber et al., 2002). Nevertheless, there seemed to be a declining trend during the Late Cretaceous (Wang et al., 2014), which might be related to the enhanced weathering of basaltic provinces on continents that were drifting through the equatorial humid belt (Kent and Muttoni, 2013). To test effects of CO_2 on the Asian aridity, four experiments (x1, x2, x4, and x8, Table 1) are conducted with the CO_2 concentrations being 280, 560, 1120, and 2240 ppmv, respectively, almost bracketing the full range estimated from the geological records (Wang et al., 2014). In these four experiments, the eccentricity is fixed at 0 and obliquity equals to 23.3° in order to focus on the influence of CO_2 alone. For such orbital configuration, the seasonality is still significant but is not affected by precession due to the circular orbit. Another two sets of experiments are done to test whether the orbital configuration may affect the dependence of Asian aridity on CO_2, only two CO_2 concentrations are tested in each set. In one set, the orbital configuration is the same as that of present day and CO_2 concentrations of experiments x2 and x8 are tested (experiments x2_modern and x8_modern, Table 1); in the other, the eccentricity and obliquity are set to their maximum values (0.067 and 24.5°, respectively), and precession is set such that the summer of Northern Hemisphere occurs at perihelion (experiments x1_LoLeSp and x4_LoLeSp, Table 1). For this latter set, the CO_2 concentrations of experiments x1 and x4 are tested because the model does not converge at some points on land for the same CO_2 concentration of experiment x8.

Table 1
CO_2 concentration, orbital parameters and dry area in each experiment.

Exp	CO_2 (ppmv)	Orbital parameters			Arid area[a] (10^6 km^2)
		Obliquity	Eccentricity	Perihelion	
x1	280	23.3	0	–	9.16 (4.09)
x2	560	23.3	0	–	9.27 (4.04)
x4	1120	23.3	0	–	9.30 (3.19)
x8	2240	23.3	0	–	9.43 (2.89)
x1_LoLeSp	280	24.5	0.067	270	6.87 (1.60)
x2_modern	560	1990 CE	1990 CE	1990 CE	9.63 (4.39)
x4_LoLeSp	1120	24.5	0.067	270	7.0 (0.71)
x8_modern	2240	1990 CE	1990 CE	1990 CE	9.59 (3.31)
x2_v	560	23.3	0	–	9.43 (3.49)
x2_LoLeWp	560	24.5	0.067	90	9.90 (4.67)
x2_LoLeSp	560	24.5	0.067	270	6.70 (1.15)
x2_SoLeWp	560	22	0.067	90	11.22 (6.45)
x2_SoLeSp	560	22	0.067	270	7.60 (2.48)
x2_MoLeWp	560	23.3	0.067	90	10.06 (5.57)
x2_MoLeSp	560	23.3	0.067	270	7.01 (1.73)
x2_MoMeWp	560	23.3	0.047	90	9.90 (4.96)
x2_MoMeSp	560	23.3	0.047	270	7,75 (2.47)
x2_MoSeWp	560	23.3	0.027	90	9.75 (4.51)
x2_MoSeSp	560	23.3	0.027	270	8.37 (3.20)

[a] The number of the last column represents the sum area of hyperarid, arid, semi-arid and dry sub-humid regions, and the number in the brackets the sum area of hyper-arid and arid regions. “1990 CE” represents year 1990 orbital parameters are used.

All the other sensitivity experiments are designed by perturbing the experiment x2. The first sensitivity experiment is on the vegetation distribution. According to Jiang et al. (2004) and Hasegawa et al. (2012), eolian dust deposits was widely distributed in the low- to mid-latitude Asia, different from the vegetation distribution provided by Sewall et al. (2007; Fig. 1b). To test whether this will affect the simulated climate and aridity over Asia, we remove the vegetation between 20 and 40°N and west of 100°E in Asia and set the land surface to be desert in the experiment x2_v.

Ten experiments (x2_LoLeWp, x2_LoLeSp, x2_SoLeWp, x2_SoLeSp, x2_MoLeWp, x2_MoLeSp, x2_MoMeWp, x2_MoMeSp, x2_MoSeWp, and x2_MoSeSp, Table 1) are carried out to investigate the responses of Asian aridity to the orbital perturbations. The orbital parameters, i.e. the obliquity, precession and eccentricity of the Earth, are varied within their respective ranges during the Late Cenozoic (25 Ma – now; Laskar et al., 2004). Their ranges during the Late Cretaceous were very similar to those during the Late Cenozoic (Laskar et al., 2004; Ma et al., 2017a), but uncertainties get larger for time periods more distant from now. In the experiment names, character combination “Lo” (“Mo”, or “So”) represents the large (medium, or small) obliquity with value of 24.5° (23.3°, or 22.0°), and “Le” (“Me”, or “Se”) the large (medium, or small) eccentricity with value of 0.067 (0.047, or 0.027). The character combinations “Sp” and “Wp” mean that the northern hemispheric summer and winter solstices, respectively, occur at perihelion, due to the precession of Earth's rotational axis. Thus, the difference between x2_LoLeWp and x2_SoLeWp (or x2_LoLeSp and x2_SoLeSp) shows the effects of the obliquity. The difference between x2_MoLeWp and x2_MoLeSp (x2_MoMeWp and x2_MoMeSp, or x2_MoSeWp and x2_MoSeSp) gives the effect of the precession, and the difference among x2_MoLeWp, x2_MoMeWp, and x2_MoSeWp (or x2_MoLeSp, x2_MoMeSp, and x2_MoSeSp) represents the effects of the eccentricity.

In all experiments, solar constant is reduced to 1351.47 W/m^2,

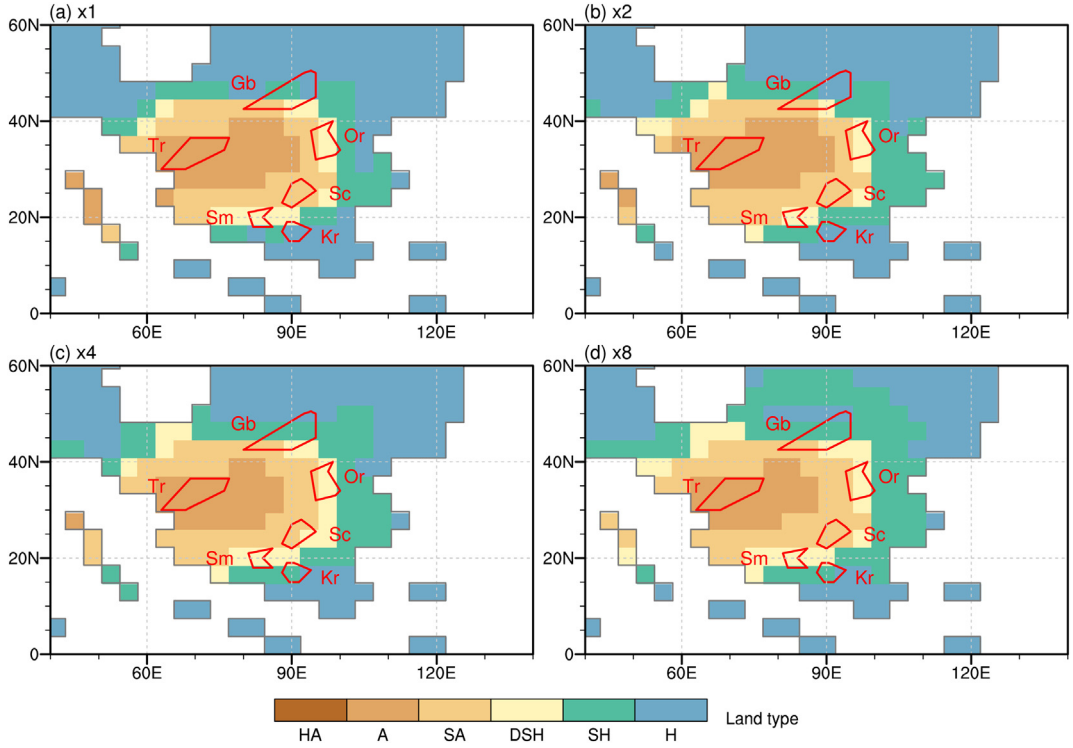

Fig. 2. The geographic distribution of land types simulated by the experiments x1 (a), x2 (b), x4 (c), and x8 (d). For the land types, H is for the humid type, SH for the semi-humid type, DSH for dry sub-humid type, SA for the semi-arid type, A for the arid type, and HA for the hyper-arid type, respectively. The each red polygon represents a basin (Hasegawa et al., 2012), and abbreviated basin names are as follows: Gb = Gobi, Tr = Tarim, Or = Ordos, Sc = Sichuan, Sm = Simao, Kr = Khorat. (For interpretation of the references to color in this figure legend, the reader is referred to the web version of this article.)

about 0.7% lower than the present-day solar constant of 1361 W/m^2 (Gough, 1981; Kopp and Lean, 2011). The concentrations of CFCs are set to 0, and CH_4 and N_2O are set 760 ppbv and 270 ppbv, respectively. All the other atmospheric constituents, including O_3 and aerosols are set to preindustrial level, i.e. the default values of the CESM1.2.

The experiments x1, x2, and x4 are all run for 2700 model years, the experiment x8 is branched from year 2701 of the experiment x4 and continued for another 1000 model years. The remaining each experiment is branched from the quasi-equilibrium state of the experiment of circular orbit with the same CO_2 concentration, and continued for another 600 model years, which is long enough for the surface climate to reach quasi-equilibrium. Because the orbit configuration evolves slowly (in timescale of 10,000 years) and the surface climate equilibrates with the perturbed orbital configuration quickly, we do not need to simulate the climate through a whole orbital cycle; simulating climates at a few representative orbital configurations should suffice, justifying our experimental design above. The last 100-year data from each experiment are analyzed and presented herein.

2.3. Aridity classification

In this study, we classify the land type according to the aridity index (AI), defined as the ratio of the annual rainfall (PT) to the annual potential evapotranspiration (PET). The greater (less) the AI, the wetter (drier) the climate. The daily PET is calculated using the Penman approach, based on the temperature, relative humidity, wind speed and available energy (i.e. the difference between the surface net radiation and the soil heat flux, Penman, 1948)

$$\mathrm{PET} = \frac{\Delta(R_n - G)}{\Delta + \gamma} + \frac{\gamma f(U)(e_o - e_a)}{\Delta + \gamma} \quad (1)$$

where Δ is the slope of the saturation vapor pressure curve at air temperature (kPa °C^{-1}), γ is the psychrometric constant (kPa °C^{-1}); R_n and G are, repectively, net radiation at land surface and soil heat flux in the ground converted to vaporization fluxes (in unit mm d^{-1}) with the help of latent heat of evaporation; e_o and e_a are the saturation and actual water vapor pressure of the air (kPa), respectively; $f(U)$ is the so-called Rome wind function (Brutsaert, 1982)

$$f(U) = 2.6(1 + 0.54U) \quad (2)$$

where U is the 2 m wind speed (m/s), and $f(U)$ is given in mm d^{-1} kPa^{-1}. This approach of calculating the PET is also widely used in the analyses of modern climate (Ma et al., 2015; Maes et al., 2018; Milly and Dunne, 2016).

The land surface is classified into six types according to their AI values, namely hyper-arid (HA; AI $<$ 0.05), arid (A; 0.05 $\leq$ AI $<$ 0.2), semi-arid (SA; 0.2 $\leq$ AI $<$ 0.5), dry sub-humid (DSH, 0.5 $\leq$ AI $<$ 0.65), semi-humid (SH, 0.65 $\leq$ AI $<$ 1.0) and Humid (H, AI $\geq$ 1.0). The first four types are normally considered to represent dry conditions, and remaining two represent wet conditions. This kind of land climate classification is extensively used in the studies of the modern and past climate changes (Feng and Fu, 2013; Liu et al., 2018; Ma et al., 2017b).

3. Results

3.1. Influence of CO_2 on the aridity of Asia

The global mean surface temperature is 18.4 °C, 21.7 °C, 23.8 °C, and 26.6 °C for the experiments x1, x2, x4, and x8, respectively. For experiment x2, which we will take as the control experiment in the following analyses, the annual mean surface temperature near the equator and poles are ~30 °C and ~0 °C, respectively, in line with geologic records (Spicer and Herman, 2010). The dryland, i.e. those areas with aridity type HA, A, SA or DSH, is mainly located over the mid- to low-latitude of Asia, South America, and Africa (Fig. 1c), in

good accordance with the vegetation distribution shown in Fig. 1b. The global land type distribution in the experiments x1, x4, and x8 are similar to that in the experiment x2 (not shown but the Asian aridity is analyzed in detail below). This gives us confidence in the model's ability in simulating the land types for the Late Cretaceous.

Most of the area between 20 and 45°N of Asia were dry during the Late Cretaceous, only the east coastal region is semi-humid or humid (Fig. 2). This is very different from the aridity distribution of today, and is consistent with reconstructions (Fang et al., 2016; Hasegawa et al., 2012; Jiang et al., 2008; Herman and Spicer, 2010; Spicer and Herman, 2010). The result is also comparable with modeling outputs of Sellwood and Valdes (2006). Interestingly, the variation of CO_2 has little influence on the simulated land type distribution or pattern over the Late Cretaceous Asia (Fig. 2). The land type patterns in these four experiments are generally consistent with the reconstructed vegetation distribution (Fig. 1b) that has been used as a priori boundary condition. Further test by replacing the vegetation on the dry land with desert (in experiment x2_v) shows negligible influence on the simulated land type. Therefore, we did not bother changing the boundary condition in other modeling experiments.

The area of each land type over the paleo-Asian continent between 20 and 40°N is calculated for individual experiment and presented in Fig. 3a. For all the four experiments x1, x2, x4 and x8, there is no hyperarid region in Asia. The sums of dryland area are almost the same (~9.0–9.5 *10^6 km^2, Table 1, Fig. 3a) among these four experiments; the average AI over the region between 20 and 40°N Asia increases by only 0.004 as CO_2 concentration is increased by 8 fold (Fig. 3b). The area belonging to the arid type, however, has a clearly decreasing trend as CO_2 is increased, but the semi-arid area shows an increasing trend (Table 1, Fig. 3a). Such influence of CO_2 on the extent of Asian dry land is insensitive to orbital configurations (Fig. S1).

The results are probably consistent with previous modeling study by Chen et al. (2013), who showed that the climate cooling could expand the dryland area in Asia during the Cretaceous. Exact comparison is hampered because they diagnosed the dryland region by only looking at whether evaporation is greater than precipitation, which is a coarse classification and sometimes less appropriate than the aridity index employed here. Our results are consistent with the decrease of arid area, increase of semi-arid area and the expansion of dryland during the past 60 years and the future 100 years due to global warming (Huang et al., 2016a, 2016b).

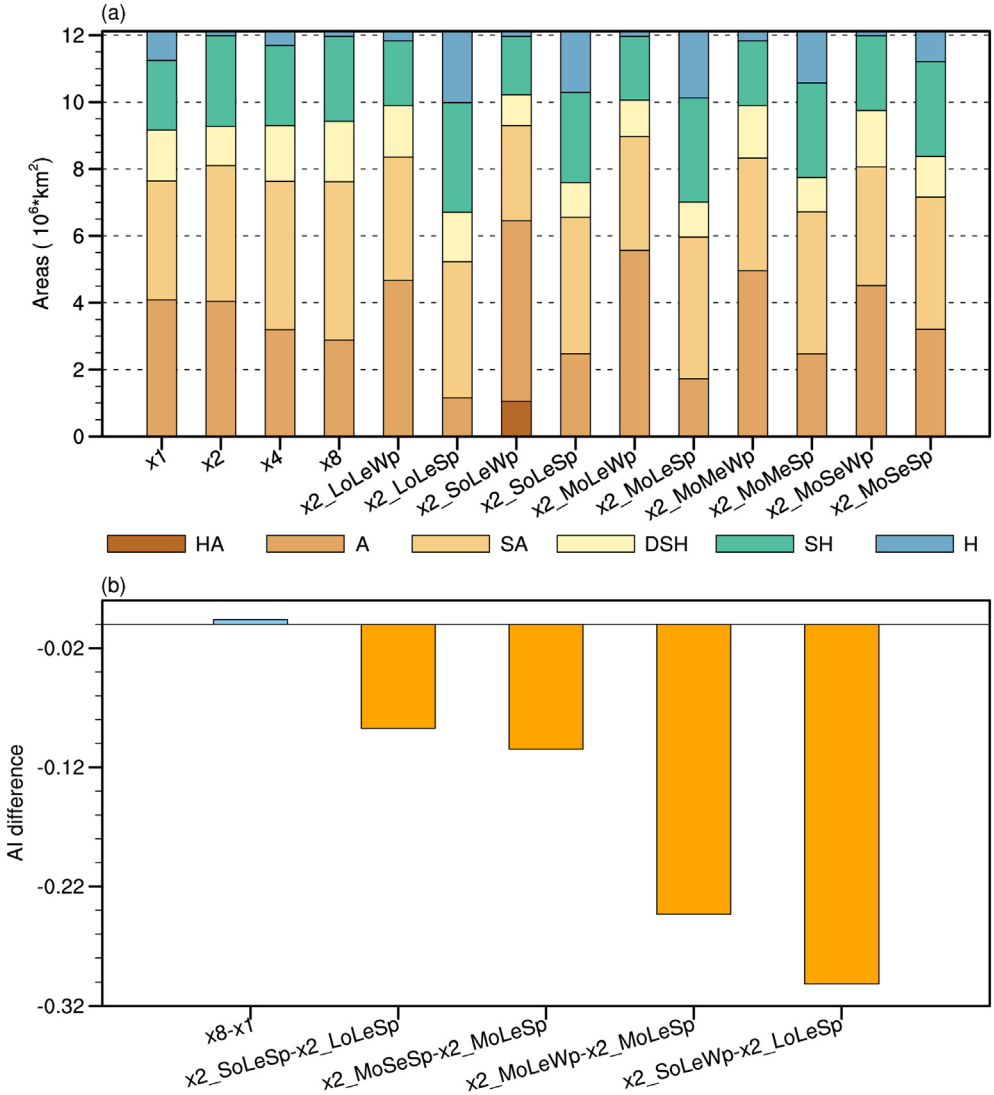

Fig. 3. The area (units: 10^6 km^2, each color corresponds to that in Fig. 2) of the each arid/humid type in every experiment over the area of 20–40°N, 40–120°E (a), and the area averaged AI difference over the corresponding region (b). In (a), HA is for the hyper-arid type, A for the arid type, SA for the semi-arid type, DSH for the dry sub-humid type, SH for the semi-humid type, and H for the humid type, respectively.

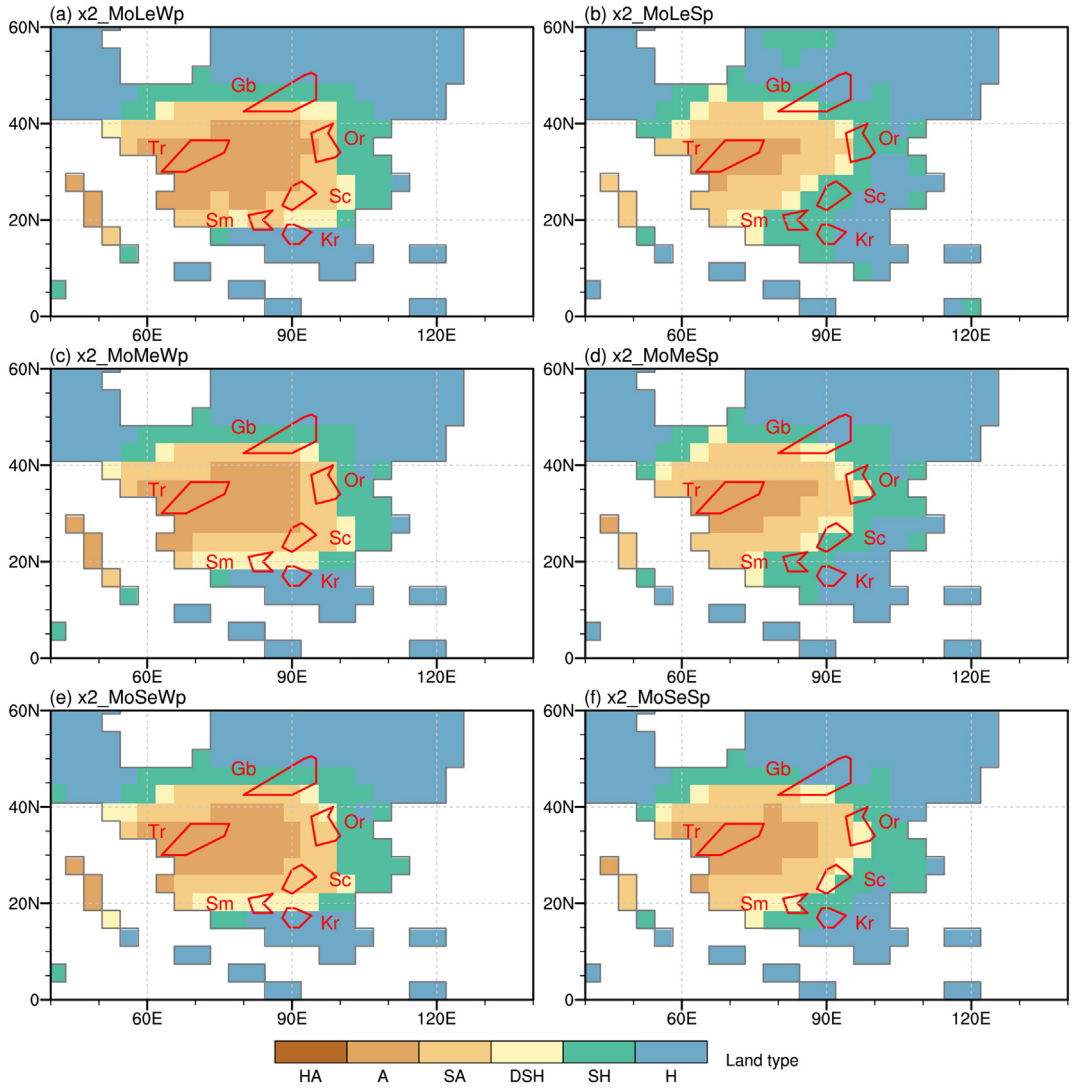

Fig. 4. Same as Fig. 2, but for the experiments x2_MoLeWp (a), x2_MoLeSp (b), x2_MoMeWp (c), x2_MoMeSo (d), x2_MoSeWp (e), and x2_MoSeSp (f).

3.2. Influence of orbital configuration on the aridity of Asia

The area of dryland over Asia is always smaller when the summer occurs at perihelion than when it occurs at aphelion (controlled by precession; compare the right column with the left column in both Figs. 4 and 5). The magnitude of the difference, however, is dependent on the eccentricity; the larger the eccentricity, the larger the difference in dryland area between different precession settings. When eccentricity is small (0.027), the Ordos Basin changes from dominantly semi-arid when summer is at aphelion to dry sub-humid when summer is at perihelion, similarly for the southern part of the Gobi Basin (compare Fig. 4e and f), while for large eccentricity (0.067), the Ordos Basin, Sichuan Basin, Simao Basin, and the southern Gobi Basin all change from dominantly semi-arid to semi-humid (compare Fig. 4a and b).

The influence of eccentricity on the aridity of Asia, if precession is fixed, is mild. If the northern hemispheric summer occurs at aphelion, the dryland area decreases slightly with the decrease of eccentricity (Figs. 3a, 4a, c and e); while if it occurs at perihelion, the dryland area increases with the decrease of eccentricity (Figs. 3a, 4b, d and f).

The dryland area over the Asia shrinks moderately towards the west when the obliquity of the Earth increases, independent of precession (Fig. 5). For instance, the hyper-arid area is ~$1.0*10^6$ km^2 in the experiment x2_SoLeWp (Figs. 3a and 5c) which has a small obliquity (22.0°), while this type of dryland disappears when the obliquity is increased to 24.5° (Fig. 5a). Therefore, all three orbital parameters affect the land type pattern of the Asia.

In contrast to CO_2, which affects mainly the area of arid and semi-arid land with little influence on area of total dryland (Fig. 3a), orbital parameters have significant influence on the areas of arid and semi-arid land and total dryland. The driest case is obtained when the summer occurs at aphelion, obliquity is small and eccentricity is at its maximum (experiment x2_SoLeWp, Figs. 3a and 5c), for which the total dryland area over 20–40°N Asia is 11.22 $*10^6$ km^2; the wettest case is obtained when the summer occurs at perihelion, obliquity is large and eccentricity is at its maximum (experiment x2_LoLeSp, Figs. 3a and 5b), for which the total dryland area is 6.70 $*10^6$ km^2. If only the land drier than arid type (inclusive) is considered, then the dry area is 6.45* 10^6 km^2 and 1.15*10^6 km^2 for the driest and wettest cases, respectively, a change of almost 6-fold. The change of the average AI over 20–40°N zone of paleo-Asia due to orbital variations is two orders of magnitude larger than those due to CO_2 variations (Fig. 3b).

4. Mechanism

As described in the previous section, the area of arid land decreases with increasing CO_2 concentration. This has been analyzed by Chen et al. (2013) to be due to larger increase of precipitation than evaporation, thus would not be discussed further here. We mainly focus on

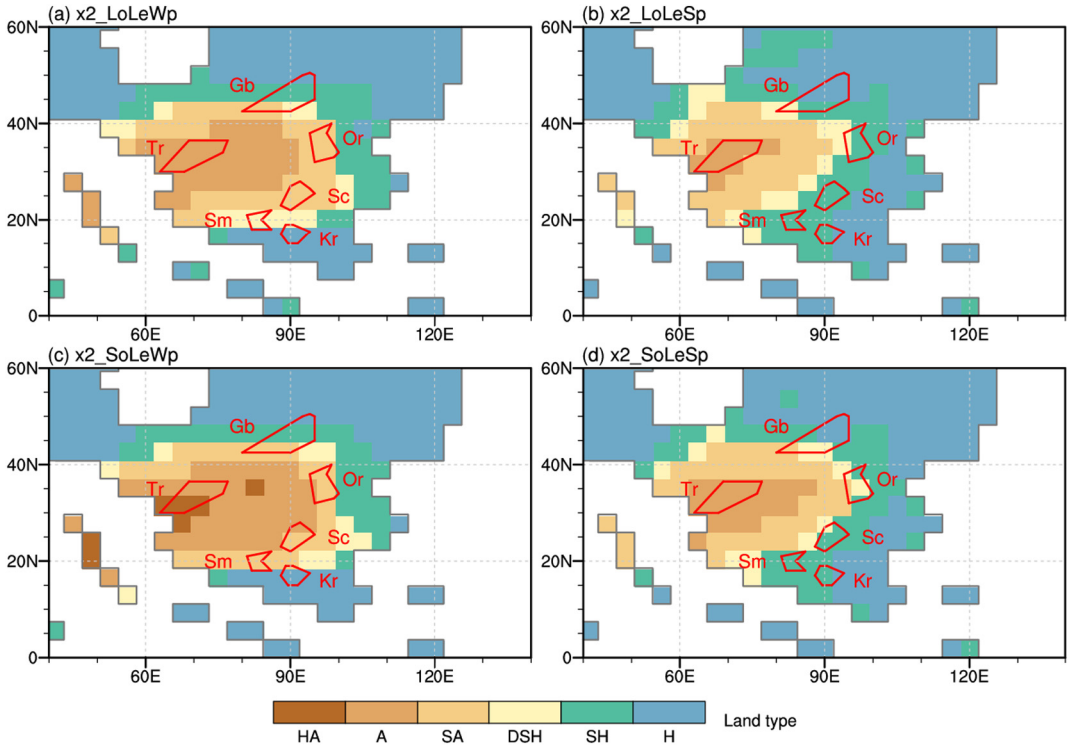

Fig. 5. Same as Fig. 2, but for the experiments x2_LoLeWp (a), x2_LoLeSp (b), x2_SoLeWp (c), and x2_SoLeSp (d).

the effect of orbital configuration.

4.1. The change of insolation

The incoming solar insolation at the top of atmosphere (STOA) averaged over 20–40°N Asia changes significantly with orbital parameters (Fig. 6). The change of STOA induced by the variation of obliquity between 22° and 24.5° is relatively small, with the greatest value being ~20 W/m^2 (Fig. 6a and b). The variation of eccentricity between 0.067 and 0.027 can lead to a larger change of STOA, ~50 W/m^2 (Fig. 6c and d). The change of precession has the largest impact on STOA, especially when the eccentricity is large; it can reach over 100 W/m^2 when the eccentricity is at its maximum value (0.067, Fig. 6e), and ~50 W/m^2 even when the eccentricity is modest (0.027, Fig. 6f). Note that the northern hemispheric summer always occurs around June in the model no matter what the precession is, so that the changes of orbital parameters all have large influence on June insolation over Asia (Fig. 6). It is well known that the change of summer insolation has large influence on the precipitation over land. For example, the wetting of Sahara during the mid-Holocene (9–6 ka) has been successfully simulated by most climate models and attributed to the increased summer insolation over Sahara during that time (Braconnot et al., 2007; Jiang et al., 2015). This mechanism should also apply to the Asia during the Late Cretaceous.

4.2. The change of precipitation and evapotranspiration

The low- to mid-latitude Asian climate during the Late Cretaceous is clearly monsoonal, similar to that of modern; southwesterly winds are prevalent during summer and northeasterly/westerly winds during winter, and the summer precipitation dominates the annual precipitation (Fig. S2). The summer winds bring large amount of precipitation to the southern and eastern Asia, but not to the western part where the water vapor mainly comes from the northwest (Fig. S2c). The patterns are similar to those obtained by Chen et al. (2013). This basic pattern of wind and precipitation determines the general aridity pattern in the Late Cretaceous Asia, but the severity of aridity changes with orbital parameters as shown in Figs. 4 and 5.

Both annual PT and PET change when the orbital configuration is changed. Fig. 7 shows the annual PT and PET over Asia from the two most extreme cases, i.e. the experiments x2_LoLeSp and x2_SoLeWp (see Fig. 5b and c for their respective land type patterns). Not only the annual PT is much larger in x2_LoLeSp (Fig. 7a) than in x2_SoLeWp (Fig. 7b), but also the annual PET is much smaller. The magnitude of PET is determined by relative humidity of air, surface temperature, wind speed, and available energy. Detailed analysis shows that the reduced PET in x2_LoLeSp compared to x2 is mainly due to the higher relative humidity of the air (Fig. 8c) and lower surface temperature (Fig. 8d) in the former than in the latter (not shown), while the changes of PET induced by the available energy (Fig. 8a) and wind speed (Fig. 8b) are less important. In x2_LoLeSp, the lower surface temperature is resulted from the much more low cloud, compared with x2. The conditions leading to the increased PET in x2_SoLeWp compared to x2 are almost opposite to that in x2_LoLeSp (Fig. S3). The coherent changes of annual PT and PET are observed in all the orbit-sensitivity experiments.

The changes in the strength of summer wind and precipitation correspond well with the change in summer STOA among different orbital configurations; when the summer STOA increases, both the winds and precipitation strengthen (Figs. 9 and S4). For the strongest case, i.e. experiment x2_LoLeSp, the summer precipitation increases by > 1 mm/day over most part of interested region of the Asia and > 4 mm/day in the most impacted region, relative to that in the base case x2. The speed of the 850 hPa southwesterly winds increase by approximately 2 m/s and can reach 5 m/s in the most impacted region (Fig. 9b). The change in summer precipitation is representative of the change in annual mean since it dominates the annual precipitation (Fig. S2). The relationship between the orbit-induced solar insolation and the Asian climate has been studied extensively for the Late Quaternary, by both observational (Wang et al., 2008) and modeling means (Kutzbach et al., 2008; Bosmans et al., 2018); the Asian monsoonal precipitation increases when the incoming solar insolation in summer becomes

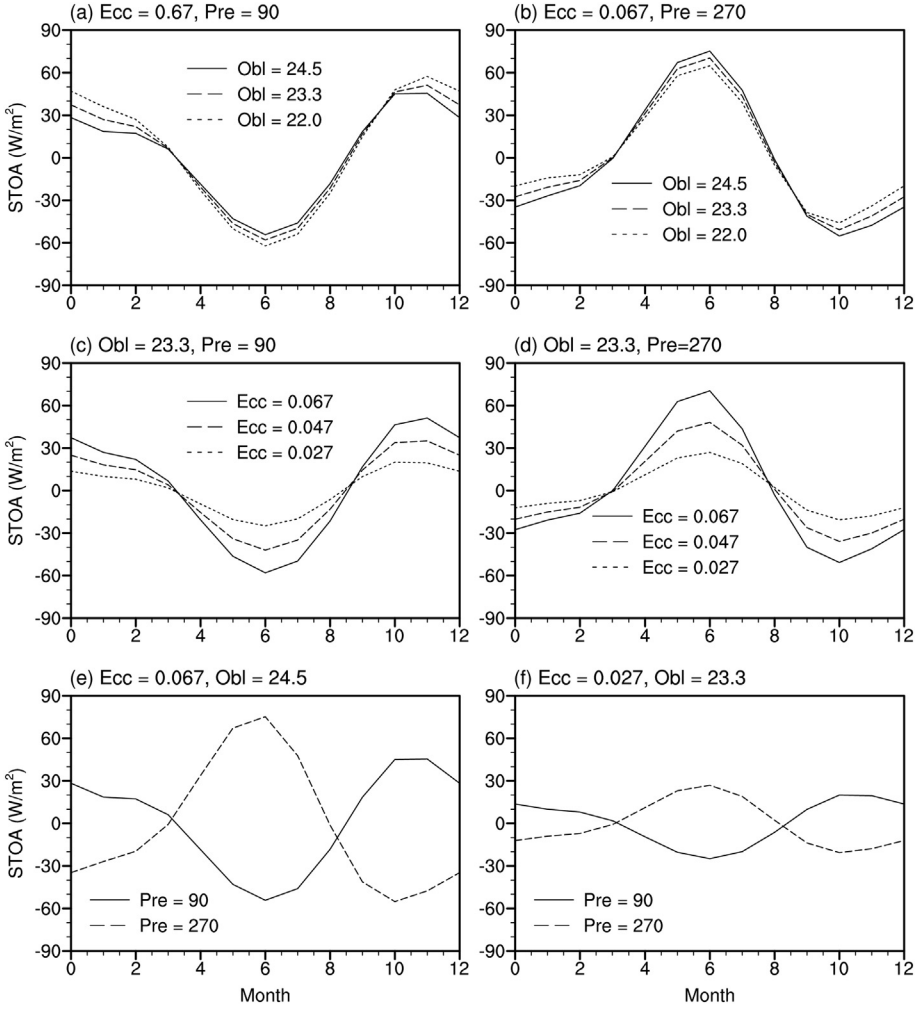

Fig. 6. Changes of the STOA over the latitudes 20–40°N between every orbital configuration and the one in the experiment x2.

strong. It is the same as what is demonstrated herein for the Late Cretaceous, but we further show that it could substantially affect the land type pattern over Asia at this time period.

Continental topography can have a significant effect on the Asian climate (Zhang et al., 2017, 2018) and land type pattern (Su et al., 2018). However, it is unlikely to vary periodically within the time interval of interest in this study. On the other hand, its change may influence how the Asian climate responds to orbital variations (Liu et al., 2003). The topography of the coastal mountains along the East Asian margin during the Late Cretaceous was distinctly different from that of the present (Zhang et al., 2016), and might have changed significantly in million year timescale. The coupled climatic effect of this topographic change and the orbital variations is certainly worthy of investigation in the near future.

5. Conclusions

The land type pattern in Asia during the Late Cretaceous and its sensitivity to both CO_2 concentrations and orbital configurations are studied using an atmosphere-ocean general circulation model. The

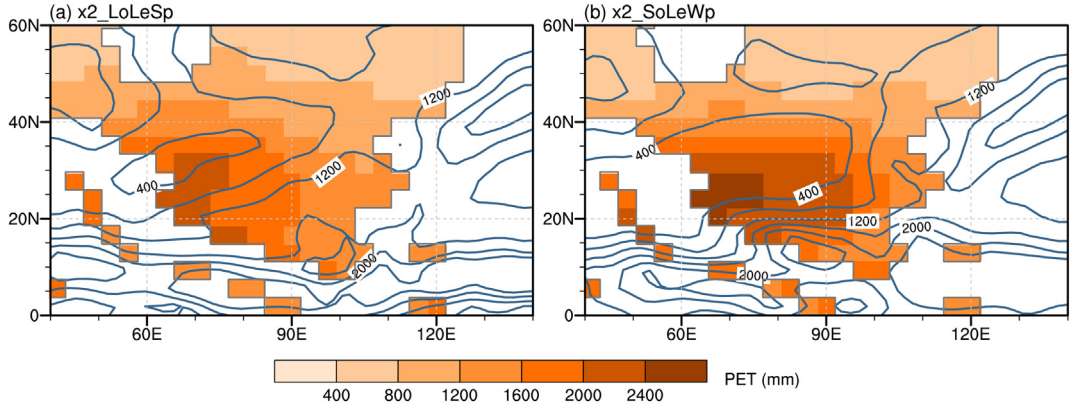

Fig. 7. Annual mean rainfall (contours, units: mm) and potential evapotranspiration (shading, units: mm) for the experiments x2_LoLeSp (a) and x2_SoLeWp (b).

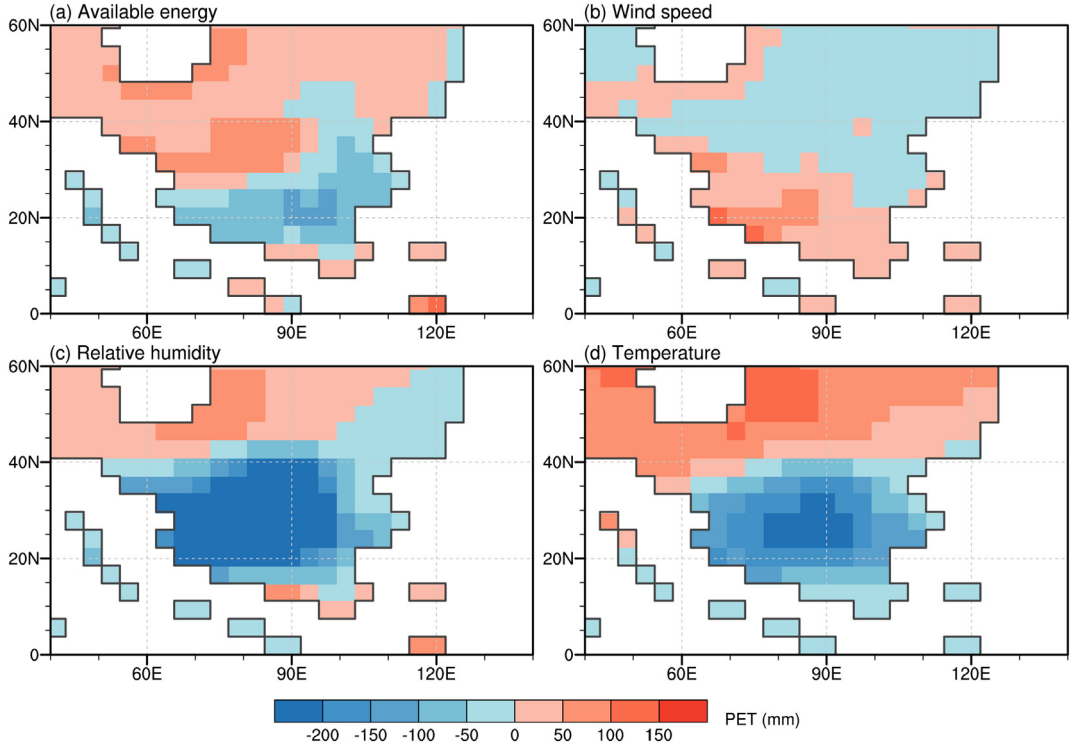

Fig. 8. Changes of annual PET (units: mm) induced by the available energy (a), wind speed (b), relative humidity (c), and temperature (d) in the experiment x2_LoLeSp compared with the counterpart in the experiment x2.

global land type pattern obtained by the simulations is in good agreement with the reconstructed vegetation distribution. Simulation results show that the region between 20 and 45°N of Asia was generally dry during the Late Cretaceous, except the southeastern and easternmost parts which were under influence of strong summer precipitation. Although the area of hyperarid and arid land increases slightly with decreasing CO_2, consistent with previous study, the total area of dry land changes little with CO_2. In contrast, it changes significantly with the variation of orbital parameters. Increasing obliquity of Earth always reduces the dry land area over Asia (Table 1); variation of precession

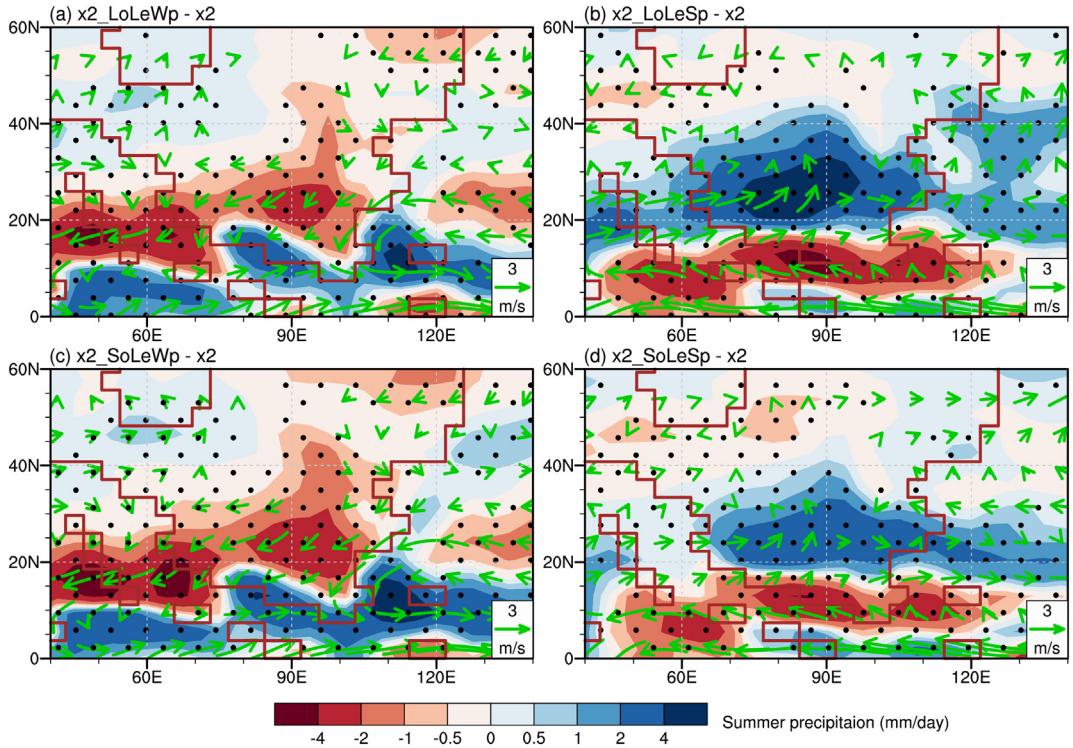

Fig. 9. Changes of summer precipitation (shaded; units: mm/day) and 850 hPa winds (vectors, units: m/s) between experiment x2_LoLeWp and x2 (a), x2_LoLeSp and x2 (b), x2_SoLeWp and x2 (c), and x2_SoLeSp and x2 (d). Only the areas with confidence levels > 95% (using the Student's *t*-test) for the precipitation are dotted.

may either reduce or enlarge the dry land area depending on whether the summer occurs closer to or farther from the perihelion. The influence of precession on Asian climate is only significant when the eccentricity of Earth orbit is non-zero, and increases with eccentricity. The driest case is obtained when the obliquity is the smallest (22°), the eccentricity is largest (0.067) and the summer occurs at aphelion (experiment x2_SoLeWp) and the wettest case is obtained when the obliquity is the largest (24.5°), the eccentricity is largest (0.067) and the summer occurs at perihelion (experiment x2_LoLeSp). The area of land drier than dry sub-humid (arid) is 11.22 (6.45) $*10^6\,km^2$ in the driest case (experiment x2_SoLeWp), but reduces to 6.70 (1.15) $*10^6\,km^2$ in the wettest case (experiment x2_LoLeSp). The large influence of orbital configuration on the Asian land type is because of the dominance of summer precipitation on the annual precipitation in this region; the strength of summer wind and precipitation is sensitive to the summer solar insolation received locally, which itself is sensitive to orbital configurations. Therefore, our results suggest that the mid- to low-latitude Asia went through substantial dry-humid cycles on orbital scales during the Late Cretaceous, similar to what has been happening in North Africa during the Late Miocene-Pleistocene (e.g. Niedermeyer et al., 2010; Vallé et al., 2017).

Supplementary data to this article can be found online at https://doi.org/10.1016/j.palaeo.2019.06.003.

Acknowledgments

We sincerely thank Dr. Jacob Ogilvie Sewall (Kutztown University of Pennsylvania) for providing the paleogeography and paleovegetation data, Prof. Dabang Jiang (Institute of Atmospheric Physics, Chinese Academy of Sciences), Dr. Baohuang Su (Institute of Atmospheric Physics, Chinese Academy of Sciences), Dr. Ning Ma (Institute of Tibetan Plateau Research, Chinese Academy of Sciences) for helpful discussions, and two anonymous reviewers for their insightful comments. This study was co-supported by the Strategic Priority Research Program of Chinese Academy of Sciences (grant XDA20070201), National Natural Science Foundation of China (grants 41790450 and 41620104002), and the China Postdoctoral Science Foundation (grant 2017M611015). The model simulations were performed on TianHe-2, thanks for the support of National Supercomputer Center in Guangzhou (NSCC-GZ).

References

Bice, K.L., Norris, R.D., 2002. Possible atmospheric CO2 extremes of the Middle Cretaceous (late Albian–Turonian). Paleoceanography 17, 1070.
Bornemann, A., Norris, R.D., Friedrich, O., Beckmann, B., Schouten, S., Damsté, J.S.S., Vogel, J., Hofmann, P., Wagner, T., 2008. Isotopic evidence for glaciation during the cretaceous supergreenhouse. Science 319, 189–192.
Bosmans, J.H.C., Erb, M.P., Dolan, A.M., Drijfhout, S.S., Tuenter, E., Hilgen, F.J., Edge, D., Pope, J.O., Lourens, L.J., 2018. Response of the Asian summer monsoons to idealized precession and obliquity forcing in a set of GCMs. Quat. Sci. Rev. 188, 121–135.
Braconnot, P., Otto-Bliesner, B., Harrison, S., Joussaume, S., Peterchmitt, J.Y., Abe-Ouchi, A., Crucifix, M., Driesschaert, E., Fichefet, T., Hewitt, C.D., Kageyama, M., Kitoh, A., Laîné, A., Loutre, M.F., Marti, O., Merkel, U., Ramstein, G., Valdes, P., Weber, S.L., Yu, Y., Zhao, Y., 2007. Results of PMIP2 coupled simulations of the Mid-Holocene and Last Glacial Maximum – part 1: experiments and large-scale features. Clim. Past 3, 261–277.
Brutsaert, W., 1982. Evaporation Into the Atmosphere: Theory. History, and Applications. 299 pp., Spring, N. Y.
Chen, J., Zhao, P., Wang, C., Huang, Y., Cao, K., 2013. Modeling East Asian climate and impacts of atmospheric CO2 concentration during the Late Cretaceous (66Ma). Palaeogeogr. Palaeoclimatol. Palaeoecol. 385, 190–201.
Danabasoglu, G., Bates, S.C., Briegleb, B.P., Jayne, S.R., Jochum, M., Large, W.G., Peacock, S., Yeager, S.G., 2012. The CCSM4 ocean component. J. Clim. 25, 1361–1389.
Fang, X., Song, C., Yan, M., Zan, J., Liu, C., Sha, J., Zhang, W., Zeng, Y., Wu, S., Zhang, D., 2016. Mesozoic litho- and magneto-stratigraphic evidence from the central Tibetan Plateau for megamonsoon evolution and potential evaporites. Gondwana Res. 37, 110–129.
Feng, S., Fu, Q., 2013. Expansion of global drylands under a warming climate. Atmos. Chem. Phys. 13, 10081–10094.
Fiorella, R.P., Sheldon, N.D., 2017. Equable end Mesoproterozoic climate in the absence of high CO2. Geology 45, 231–234.
Forster, A., Schouten, S., Moriya, K., Wilson, P.A., Sinninghe Damsté, J.S., 2007. Tropical warming and intermittent cooling during the Cenomanian/Turonian oceanic anoxic event 2: sea surface temperature records from the equatorial Atlantic. Paleoceanography 22, PA1219.
Frieling, J., Gebhardt, H., Huber, M., Adekeye, O.A., Akande, S.O., Reichart, G.-J., Middelburg, J.J., Schouten, S., Sluijs, A., 2017. Extreme warmth and heat-stressed plankton in the tropics during the Paleocene-Eocene Thermal Maximum. Sci. Adv. 3.
Gao, Y., Ibarra, D.E., Wang, C., Caves, J.K., Chamberlain, C.P., Graham, S.A., Wu, H., 2015. Mid-latitude terrestrial climate of East Asia linked to global climate in the Late Cretaceous. Geology 43, 287–290.
Gough, D.O., 1981. Solar interior structure and luminosity variations. Sol. Phys. 74, 21–34.
Hasegawa, H., Tada, R., Ichinnorov, N., Minjin, C., 2009. Lithostratigraphy and depositional environments of the Upper Cretaceous Djadokhta Formation, Ulan Nuur basin, southern Mongolia, and its paleoclimatic implication. J. Asian Earth Sci. 35, 13–26.
Hasegawa, H., Tada, R., Jiang, X., Suganuma, Y., Imsamut, S., Charusiri, P., Ichinnorov, N., Khand, Y., 2012. Drastic shrinking of the Hadley circulation during the mid-Cretaceous Supergreenhouse. Clim. Past 8, 1323–1337.
Herman, A.B., Spicer, R.A., 1996. Palaeobotanical evidence for a warm Cretaceous Arctic Ocean. Nature 380, 330.
Herman, A.B., Spicer, R.A., 2010. Mid-Cretaceous floras and climate of the Russian high Arctic (Novosibirsk Islands, Northern Yakutiya). Palaeogeogr. Palaeoclimatol. Palaeoecol. 295, 409–422.
Huang, J., Ji, M., Xie, Y., Wang, S., He, Y., Ran, J., 2016a. Global semi-arid climate change over last 60 years. Clim. Dyn. 46, 1131–1150.
Huang, J., Yu, H., Guan, X., Wang, G., Guo, R., 2016b. Accelerated dryland expansion under climate change. Nat. Clim. Chang. 6, 166–171.
Huber, B.T., Norris, R.D., MacLeod, K.G., 2002. Deep-sea paleotemperature record of extreme warmth during the Cretaceous. Geology 30, 123–126.
Hunke, E., Lipscomb, W., 2008. CICE: The Los Alamos sea ice model user's manual, version 4. Los Alamos National Laboratory Tech. Rep. In: LA-CC-06-012.
Jenkyns, H.C., Forster, A., Schouten, S., Sinninghe Damste, J.S., 2004. High temperatures in the Late Cretaceous Arctic Ocean. Nature 432, 888–892.
Jerzykiewicz, T., Russell, D.A., 1991. Late Mesozoic stratigraphy and vertebrates of the Gobi Basin. Cretac. Res. 12, 345–377.
Jiang, X., Pan, Z., Fu, Q., 2001. Primary study on pattern of general circulation of atmosphere before uplift of the Tibetan Plateau in eastern Asia. Sci. China Ser. D Earth Sci. 44, 680–688.
Jiang, X., Pan, Z., Xie, Y., Li, M., 2004. Cretaceous desert cycles, wind direction and hydrologic cycle variations in Ordos Basin: evidence for Cretaceous climatic unequability. Sci. China Ser. D Earth Sci. 47, 727.
Jiang, X., Pan, Z., Xu, J., Li, X., Xie, G., Xiao, Z., 2008. Late Cretaceous aeolian dunes and reconstruction of palaeo-wind belts of the Xinjiang Basin, Jiangxi Province, China. Palaeogeogr. Palaeoclimatol. Palaeoecol. 257, 58–66.
Jiang, D., Tian, Z., Lang, X., 2015. Mid-Holocene global monsoon area and precipitation from PMIP simulations. Clim. Dyn. 44, 2493–2512.
Kent, D.V., Muttoni, G., 2013. Modulation of Late Cretaceous and Cenozoic climate by variable drawdown of atmospheric pCO2 from weathering of basaltic provinces on continents drifting through the equatorial humid belt. Clim. Past 9, 525–546.
Kopp, G., Lean, J.L., 2011. A new, lower value of total solar irradiance: evidence and climate significance. Geophysical Research Letters 38. In: n/a-n/a.
Kutzbach, J.E., Liu, X., Liu, Z., Chen, G., 2008. Simulation of the evolutionary response of global summer monsoons to orbital forcing over the past 280,000 years. Clim. Dyn. 30, 567–579.
Laskar, J., Robutel, P., Joutel, F., Gastineau, M., Correia, A.C.M., Levrard, B., 2004. A long-term numerical solution for the insolation quantities of the Earth. A&A 428, 261–285.
Lawrence, D.M., Oleson, K.W., Flanner, M.G., Fletcher, C.G., Lawrence, P.J., Levis, S., Swenson, S.C., Bonan, G.B., 2012. The CCSM4 land simulation, 1850–2005: assessment of surface climate and new capabilities. J. Clim. 25, 2240–2260.
Liu, X., Kutzbach, J.E., Liu, Z., An, Z., Li, L., 2003. The Tibetan Plateau as amplifier of orbital-scale variability of the East Asian monsoon. Geophys. Res. Lett. 30, 1839.
Liu, Y., Peltier, W.R., Yang, J., Vettoretti, G., 2013. The initiation of Neoproterozoic “snowball” climates in CCSM3: the influence of paleocontinental configuration. Clim. Past 9, 2555–2577.
Liu, S., Jiang, D., Lang, X., 2018. A multi-model analysis of moisture changes during the last glacial maximum. Quat. Sci. Rev. 191, 363–377.
Ma, N., Zhang, Y., Szilagyi, J., Guo, Y., Zhai, J., Gao, H., 2015. Evaluating the complementary relationship of evapotranspiration in the alpine steppe of the Tibetan Plateau. Water Resour. Res. 51, 1069–1083.
Ma, C., Meyers, S.R., Sageman, B.B., 2017a. Theory of chaotic orbital variations confirmed by Cretaceous geological evidence. Nature 542, 468.
Ma, N., Niu, G.-Y., Xia, Y., Cai, X., Zhang, Y., Ma, Y., Fang, Y., 2017b. A systematic evaluation of Noah-MP in simulating land-atmosphere energy, water, and carbon exchanges over the continental United States. J. Geophys. Res. Atmos. 122, 12,245–212,268.
Maes, W.H., Gentine, P., Verhoest, N.E.C., Miralles, D.G., 2018. Potential evaporation at eddy-covariance sites across the globe. Hydrol. Earth Syst. Sci. Discuss. 2018, 1–33.
Milly, P.C.D., Dunne, K.A., 2016. Potential evapotranspiration and continental drying. Nat. Clim. Chang. 6, 946–949.
Neale, R.B., Richter, J., Park, S., Lauritzen, P.H., Vavrus, S.J., Rasch, P.J., Zhang, M., 2013. The mean climate of the Community Atmosphere Model (CAM4) in forced SST and fully coupled experiments. J. Clim. 26, 5150–5168.
Niedermeyer, E.M., Schefuß, E., Sessions, A.L., Mulitza, S., Mollenhauer, G., Schulz, M., Wefer, G., 2010. Orbital- and millennial-scale changes in the hydrologic cycle and

vegetation in the western African Sahel: insights from individual plant wax δD and δ13C. Quat. Sci. Rev. 29, 2996–3005.
Penman, H.L., 1948. Natural evaporation from open water, bare soil and grass. Proc. R. Soc. Lond. A Math. Phys. Sci. 193, 120–145.
Rosenbloom, N., Shields, C., Brady, E., Levis, S., Yeager, S., 2011. Using CCSM3 for Paleoclimate Applications. (National Center for Atmospheric Research).
Sellwood, B.W., Valdes, P.J., 2006. Mesozoic climates: general circulation models and the rock record. Sediment. Geol. 190, 269–287.
Sewall, J.O., van de Wal, R.S.W., van der Zwan, K., van Oosterhout, C., Dijkstra, H.A., Scotese, C.R., 2007. Climate model boundary conditions for four Cretaceous time slices. Clim. Past 3, 647–657.
Shields, C.A., Bailey, D.A., Danabasoglu, G., Jochum, M., Kiehl, J.T., Levis, S., Park, S., 2012. The low-resolution CCSM4. J. Clim. 25, 3993–4014.
Spicer, R.A., Herman, A.B., 2010. The Late Cretaceous environment of the Arctic: a quantitative reassessment based on plant fossils. Palaeogeogr. Palaeoclimatol. Palaeoecol. 295, 423–442.
Spicer, R.A., Ahlberg, A., Herman, A.B., Hofmann, C.-C., Raikevich, M., Valdes, P.J., Markwick, P.J., 2008. The Late Cretaceous continental interior of Siberia: a challenge for climate models. Earth Planet. Sci. Lett. 267, 228–235.
Su, B.H., Jiang, D.B., Tian, Z.P., 2018. Numerical simulation on the impact of global mountain uplift on the subtropical arid climate (in Chinese). Chin. Sci. Bull. 63, 1142–1153.
Vallé, F., Westerhold, T., Dupont, L.M., 2017. Orbital-driven environmental changes recorded at ODP Site 959 (eastern equatorial Atlantic) from the Late Miocene to the Early Pleistocene. Int. J. Earth Sci. 106, 1161–1174.
Vertenstein, M., Bertini, A., Craig, T., Edwards, J., Levy, M., Mai, A., Schollenberger, J., 2013. Cesm user's guide (cesm1. 2 release series user's guide). NCAR Technical Note.
Wang, Y., Cheng, H., Edwards, R.L., Kong, X., Shao, X., Chen, S., Wu, J., Jiang, X., Wang, X., An, Z., 2008. Millennial- and orbital-scale changes in the East Asian monsoon over the past 224,000 years. Nature 451, 1090.
Wang, C., Scott, R.W., Wan, X., Graham, S.A., Huang, Y., Wang, P., Wu, H., Dean, W.E., Zhang, L., 2013. Late Cretaceous climate changes recorded in Eastern Asian lacustrine deposits and North American Epieric sea strata. Earth Sci. Rev. 126, 275–299.
Wang, Y., Huang, C., Sun, B., Quan, C., Wu, J., Lin, Z., 2014. Paleo-CO2 variation trends and the Cretaceous greenhouse climate. Earth Sci. Rev. 129, 136–147.
Wilson, P.A., Norris, R.D., Cooper, M.J., 2002. Testing the Cretaceous greenhouse hypothesis using glassy foraminiferal calcite from the core of the Turonian tropics on Demerara Rise. Geology 30, 607–610.
Wu, H., Zhang, S., Hinnov, L.A., Jiang, G., Yang, T., Li, H., Wan, X., Wang, C., 2014. Cyclostratigraphy and orbital tuning of the terrestrial upper Santonian–Lower Danian in Songliao Basin, northeastern China. Earth Planet. Sci. Lett. 407, 82–95.
Zakharov, Y.D., Boriskina, N.G., Ignatyev, A.V., Tanabe, K., Shigeta, Y., Popov, A.M., Afanasyeva, T.B., Maeda, H., 1999. Palaeotemperature curve for the Late Cretaceous of the northwestern circum-Pacific. Cretac. Res. 20, 685–697.
Zhang, L., Wang, C., Cao, K., Wang, Q., Tan, J., Gao, Y., 2016. High elevation of Jiaolai Basin during the Late Cretaceous: implication for the coastal mountains along the East Asian margin. Earth Planet. Sci. Lett. 456, 112–123.
Zhang, R., Jiang, D., Zhang, Z., Cheng, Z., Zhang, Q., 2017. Comparison of the climate effects of surface uplifts from the northern Tibetan Plateau, the Tianshan, and the Mongolian Plateau on the East Asian climate. J. Geophys. Res. Atmos. 122, 7949–7970.
Zhang, R., Jiang, D., Ramstein, G., Zhang, Z., Lippert, P.C., Yu, E., 2018. Changes in Tibetan Plateau latitude as an important factor for understanding East Asian climate since the Eocene: a modeling study. Earth Planet. Sci. Lett. 484, 295–308.